S & M 4190

Quantifying Adhesion and Stability in Aluminum-coated Flexible Substrates for Sensor Applications via Buckling Delamination Mechanism

Shih-Chen Shi, 1* Jyun-Wei Chen, 1 and Dieter Rahmadiawan 1,2

¹Department of Mechanical Engineering, National Cheng Kung University 70101 Tainan, Taiwan ²Department of Mechanical Engineering, Universitas Negeri Padang 25173 Padang, Sumatera Barat, Indonesia

(Received March 25, 2025; accepted September 26, 2025)

Keywords: buckling delamination mechanism, tensile strain in coating, shear lag effect in PET-aluminum interfaces, lateral compressive force calculation

In this research, we explore the mechanical stability and interfacial adhesion of aluminum-coated polyethylene terephthalate substrates under tensile strain, a structure commonly used in flexible sensor platforms. Utilizing physical vapor deposition, we applied thin aluminum films and subjected them to tensile strains of 10, 15, and 20%. The resulting mechanical deformations, such as shear-lag-induced cracks and Poisson-effect-induced lateral compressive forces, were analyzed by digital microscopy and scanning electron microscopy. A buckling-delamination model based on Euler's critical load theory was used to quantify lateral compressive forces and predict interfacial failure. Results showed that regions with small buckling lengths and crack widths demonstrated high compressive forces per unit area, correlating with improved adhesion. The average compressive force per unit area was calculated as $2.7 \times 10^{-13} \text{ N/}\mu\text{m}^2$. These insights offer a predictive framework for assessing and enhancing the reliability of flexible sensor coatings under mechanical stress, crucial for the development of robust, stretchable, and wearable sensor technologies.

1. Introduction

Roll-to-roll processing is a continuous production method that processes material rolls by transferring liquid materials or inks onto a flexible substrate using a roller mechanism, also known as a coating technique.⁽¹⁾ With the rapid advancement of modern technology, there is an increasing demand for flexible and wearable sensor systems in medical diagnostics, environmental monitoring, and smart textiles. These systems require mechanically robust, stretchable materials where interfacial adhesion and coating integrity are crucial for long-term sensor reliability and performance.⁽²⁾ These flexible electronic products are primarily manufactured on a large scale using roll-to-roll process technology. According to statistics from Business Communications Company Research, the market size for roll-to-roll printed electronics

doubled from 21.2 billion USD in 2018 to 41.3 billion USD in 2023.⁽³⁾ Furthermore, a report by IDTechEx predicts that the market for flexible electronic products can grow to 73 billion USD by 2027, demonstrating the significant market potential of roll-to-roll technology.⁽⁴⁾

Adhesion is when two material surfaces are bound together through interfacial forces, including van der Waals forces, electrostatic forces, or chemical bonding. (5) The purpose of the calculations is to quantify the adhesion strength between substrates and coatings, and establish the relationship between mechanics and adhesion models. The principal derivations of the models for interface adhesion strength on polymer substrates date back to the famous Hutchinson and Suo model of 1992. (6) This model was initially applied to rigid substrates where thin films experience spontaneous delamination or compression-induced buckling delamination, using the mechanisms of crack propagation and buckling delamination based on fracture mechanics and Euler's equations to establish the theory of energy release rate for film delamination on rigid substrates. In 2004, Cordill et al. further developed this model by inducing buckling delamination in rigid substrate and film systems through nanoindentation experiments and using atomic force microscopy for imaging and measurement after buckling, deriving the mixed-mode delamination adhesion energy between the substrate and film interfaces. (7) However, measuring adhesion strength using nanoindentation on flexible polymer substrates is challenging owing to the viscoelastic behavior of polymer substrates, which do not form buckles like rigid substrate interfaces after indentation. Thus, nanoindentation experiments on polymer substrate films are limited to measuring their mechanical properties. (8–10)

In 2010, Cordill *et al.*, among others, developed a model for the adhesion energy of polymer substrate films by employing a tensile test that utilized the mechanism of buckling delamination induced by tensile forces.⁽¹¹⁾ This model explicitly targets hard films on polymer substrates and is predicated on the basis of the conditions of compressive stress caused by the Poisson effect, leading to buckling delamination. The derivation of this model considered the strain energy of both the substrate and film materials, as well as the strain energy between the delaminated layers.⁽¹¹⁾ The polymer substrate films were subjected to tensile testing to induce buckling delamination, followed by cross-sectional cutting using a focused ion beam microscope to facilitate observation. Finally, the heights and widths of the buckled sections were imaged and measured using either an atomic force microscope or a confocal laser scanning microscope.^(12–14)

In recent years, researchers have explored various strategies to enhance the mechanical performance of materials, including the incorporation of additional components to improve other properties. (15–22) For instance, Nurdin *et al.* demonstrated that carbonizing palm kernel shells with binders at optimized concentrations significantly improves the calorific value and fuel quality of the resulting charcoal briquettes. (23) This illustrates a broader principle, that is, processing parameters and interfacial interactions between material components are critical in determining final performance. Similar principles apply to the adhesion behavior of polymer—metal systems, such as polyethylene terephthalate (PET) with aluminum (Al), where adhesion strength is affected by interfacial bonding, mechanical stress, and deformation mechanisms under external loading.

Given the rising use of PET-metal interfaces in pressure, strain, and biological sensors, understanding delamination behavior under strain is essential to ensure the consistent signal

output and mechanical reliability of these flexible sensor systems. In this research, we focused on PET combined with Al deposited via physical vapor deposition (PVD) as the research subject. Different tensile strain levels were applied to form buckling delamination points. It is hypothesized that the adhesion between the hard Al layer and PET is affected by the Poisson effect, contributing to the buckling delamination mechanism. On the basis of this behavior, a method for calculating adhesion strength was developed.

This research is based on the hypothesis that the geometry of buckling delamination in metallic coatings on flexible substrates, specifically the buckling length and crack width, can be quantitatively correlated with lateral compressive forces, which in turn reflect interfacial adhesion strength. The primary objective is to develop and validate a calculation method grounded in Euler's critical load theory to determine lateral compressive forces per unit area in Al-coated PET films subjected to tensile strain.

The innovation of this work lies in introducing a force per unit area metric that integrates both buckling and crack geometry, enabling localized adhesion assessment without destructive interface separation or nanoindentation. This provides a predictive framework for designing durable flexible sensor coatings capable of withstanding operational strain.

2. Materials and Method

2.1 Materials

PET film was employed as the substrate, which was coated uniformly with a commercial acrylic paint. The acrylic-coated PET substrate was then dried in an oven. After the coating and drying procedures, Al was deposited onto the coated PET substrate via PVD using a vacuum evaporator.

2.2 Tensile tests

Tensile tests were performed in accordance with ASTM D638 Type V using a universal testing machine (AGS-X, SHIMADZU, Japan). Rectangular specimens (160 × 35 mm²) were subjected to engineering strains of 10, 15, and 20%. Strain rate and testing conditions were kept constant for all experiments to minimize viscoelastic effects in the PET substrate.

2.3 Surface and cross-sectional characterization

Following tensile deformation, the PET-Al interface was examined using a digital microscope (VHX-7000) to record surface crack widths and buckling lengths. Cross sections were observed using a multi-environment scanning electron microscope to measure coating thickness and inspect interfacial features. All measurements were performed with ImageJ software.

2.4 Buckling-delamination analysis and force calculation

Buckling delamination geometry was analyzed using the MATLAB Grabit function to extract coordinates from optical images of the Al coating after tensile deformation. The measured buckling profiles were represented mathematically to determine the characteristic wavelength and amplitude. To achieve this, the experimental data were fitted to a single-frequency sum of sines function, expressed as

$$y = \sum_{i=1}^{n} a_i \sin(b_i x + c_i), \tag{1}$$

where y represents the sum of sines, a is the amplitude, b is the frequency, and c is the phase constant of each sine wave term. The number of terms in the series, n, ranges from 1 to 8, closely related to the Fourier series described in the Fourier model fitting. In this experiment, we chose a series range of 1 term to resolve the single frequency of the waveform. Subsequently, using the buckling equation, we calculated the adhesion strength between the PET substrate and the Al coating, with the results expressed in Newtons (N).

3. Results and Discussion

3.1 Shear lag effect and crack formation in coatings

As illustrated in Fig. 1(a), the mismatch in elastic modulus between the PET substrate and the Al coating causes the mechanical stress during tensile loading to exceed the fracture strength of the Al coating, leading to the formation of surface cracks. With increasing tensile strain, stress transmission in the XY and XZ directions induces shear stress at the PET–Al interface, resulting in a shear lag effect. (14–16) This effect causes interfacial slippage between the PET substrate and the Al coating during tensile deformation, eventually leading to columnar crack propagation in the Al coating along the XY and XZ directions as strain increases.

In this research, tensile strains of 10, 15, and 20% were applied. Figures 1(b)–1(d) depict the interfacial images after the experiments. At 10% tensile strain, cracks began to form owing to the shear lag effect. As tensile strain increased, greater material elongation intensified the interfacial slippage between the PET substrate and the Al coating, leading to higher crack density.

3.2 Buckling-induced delamination of the coating

As illustrated in Fig. 2(a), the shear lag effect caused by shear stress during tensile deformation leads to interfacial adhesion failure between the PET substrate and the Al coating. Additionally, the mechanical stress generated during stretching induces the Poisson effect in the YZ direction, where the material elongates along the tensile axis and compresses in the perpendicular direction. In the PET–Al bilayer, tensile strain along the X-axis causes the PET

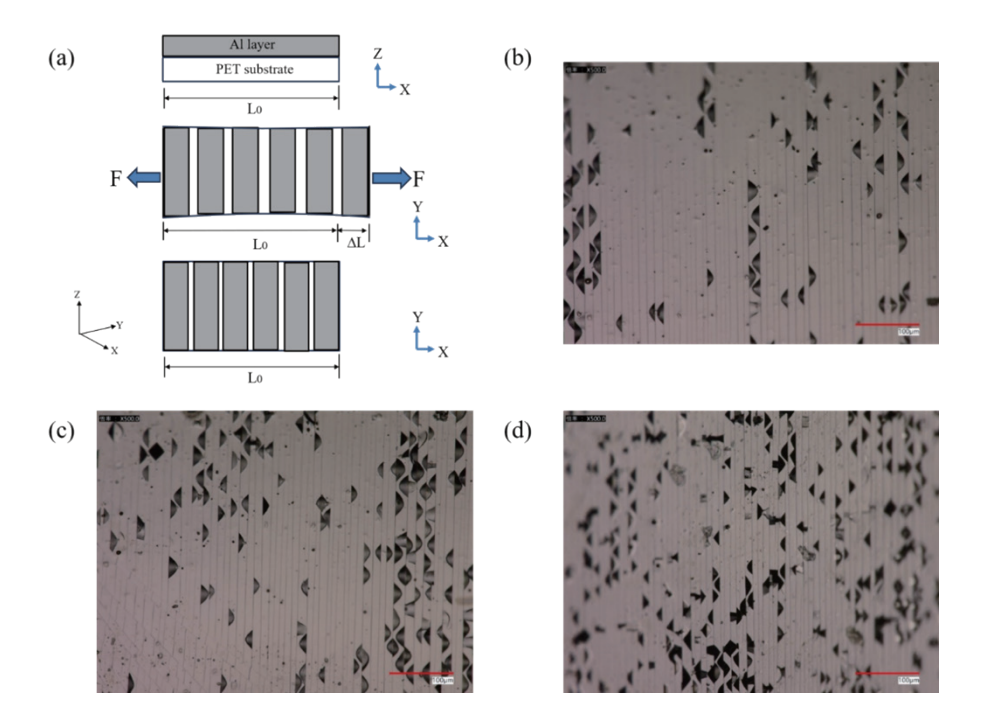


Fig. 1. (Color online) (a) Schematic representation of the shear-lag-induced crack propagation mechanism at the interface between PET and the Al coating. Interfacial images of the material in the XY direction under tensile strains of (b) 10, (c) 15, and (d) 20%.

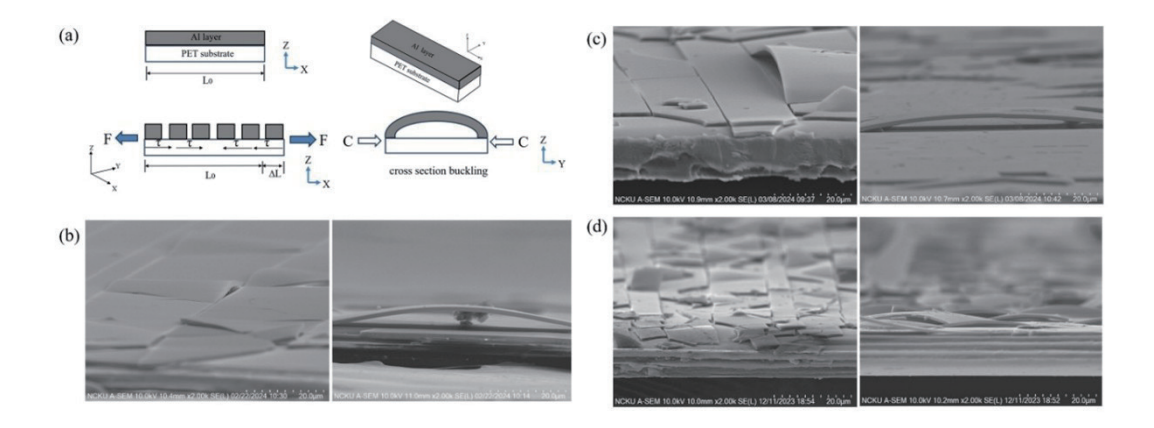


Fig. 2. (Color online) (a) Schematic diagram illustrating the buckling-induced delamination mechanism at the PET–Al interface, showing the effect of Poisson-effect-induced lateral compression. (b–d) Cross-sectional SEM images in the XZ and YZ directions for samples subjected to tensile strains of 10, 15, and 20%, respectively. Cracks in the XZ direction are attributed to shear-lag-induced interfacial slip, whereas buckling features in the YZ direction are caused by Poisson-effect-induced lateral compression. Scale bars are indicated in each panel.

substrate to contract in the transverse directions owing to its Poisson ratio. The rigid Al coating resists this contraction because of its much higher elastic modulus, resulting in a mismatch strain at the interface. This mismatch generates compressive stresses in the coating along the *Y*-axis. When these compressive stresses exceed the coating's critical buckling threshold, which is

determined by its thickness, modulus, and boundary conditions, out-of-plane deformation initiates, leading to buckling and subsequent delamination at weak adhesion sites. (24,25)

This compression creates lateral compressive stress in the YZ plane. The mismatch in elastic modulus between the PET substrate and the Al coating further amplifies this effect, resulting in buckling^(17–20) and subsequent delamination at the interface.

The cross-sectional SEM images in Figs. 2(b)–2(d) provide further insights. In the ZX direction, cracks formed owing to interfacial slippage caused by the shear lag effect. In the ZY direction, the lateral compressive stress induced by the Poisson effect resulted in buckling and delamination. These observations confirm that the primary failure mode of the Al coating under tensile strain is buckling-induced delamination.

In reference to Figs. 1(b)–1(d), initial cracks were observed at a tensile strain of 10%, driven by the shear lag effect. Subsequently, lateral compressive stress caused the formation of buckling delamination points. At this stage, the PET substrate and Al coating began to fail. As the tensile strain increased, the density of cracks at the PET–Al interface increased, accompanied by an increase in the number of buckling delamination points due to the intensifying lateral compressive stress.

3.3 Calculation of lateral compressive force in the coating using the bucklingdelamination mechanism

As shown in Fig. 3(a), during tensile deformation, cracks propagated in the Al coating owing to the shear lag effect, resulting in the formation of columnar structures after stretching. These columnar segments were subjected to lateral compressive forces, which induce buckling stress modes. On the basis of this mechanism, the lateral compressive force acting on the Al coating during buckling delamination can be determined using column buckling theory. Since the lateral compressive force was the primary factor driving the buckling delamination mechanism in the Al coating, the calculation was performed on the basis of Euler's critical load equation.

In this research, the lateral compressive force for columnar Al coatings under buckling conditions was calculated, as depicted in Fig. 3(b). The moment of inertia for the columnar Al coating is defined as

$$I = \frac{bh^3}{12} \,. \tag{2}$$

The moment of inertia (I) of the Al coating was defined in terms of its crack width (b) and thickness (h). Using this relationship, we derived the lateral compressive force exerted on the Al coating using Euler's critical load equation [Eq. (3)].

$$C = \frac{n^2 \pi^2 EI}{I^2} \tag{3}$$

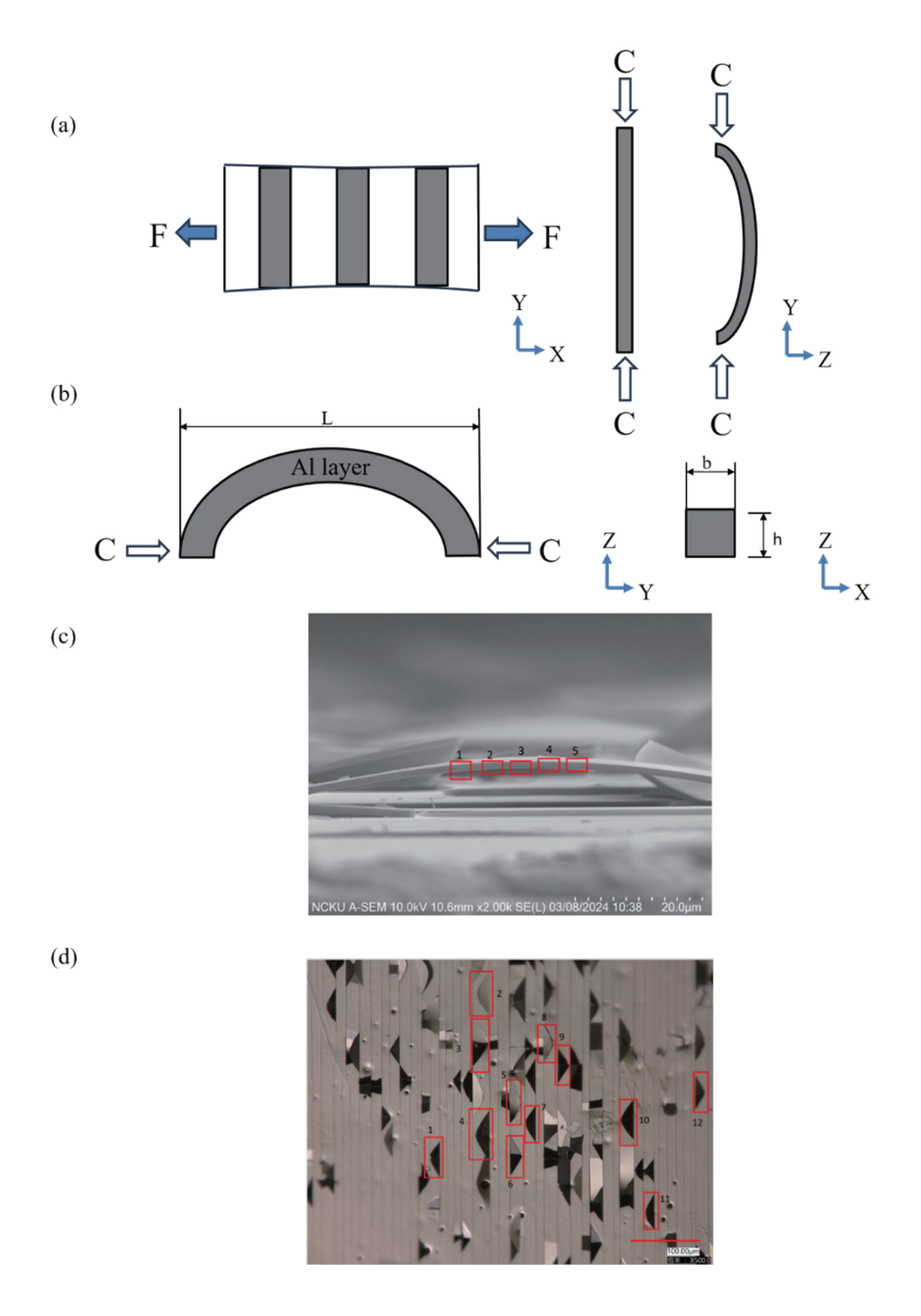


Fig. 3. (Color online) (a) Schematic representation of the columnar formation mechanism in the Al coating, (b) illustration of the moment of inertia for the columnar Al coating, (c) SEM image indicating the measurement positions for Al coating thickness, and (d) digital microscopy image identifying the calculation points for buckling delamination in the Al coating.

The lateral compressive force was computed by measuring buckling delamination points by digital microscopy and MATLAB frequency analysis. The buckling length and crack width were recorded, and an elastic modulus of 70 GPa for Al was incorporated into the calculations. The results provided key insights into how mechanical stress affects coating stability. As shown in Table 1, the average lateral compressive force during buckling delamination is 2.9×10^{-10} N. The

ID	Width (μm)	Buckling length (µm)	Frequency	Area (μm²)	Compressive force (×10 ⁻¹ N)	Unit area compressive force (×10 ⁻¹ N/µm ²)
1	13	50	1.043	650	2.4	3.7
2	25	58	1.011	1450	3.2	2.2
3	25	65	1.002	1625	2.5	1.5
4	25	67	0.951	1675	2.1	1.3
5	20	60	0.974	1200	2.2	1.8
6	20	59	1.002	1180	2.4	2.1
7	18	50	1.038	900	3.3	3.6
8	20	51	0.986	1020	3.1	3.1
9	19	50	1.008	950	3.2	3.4
10	22	55	1.014	1210	3.1	2.6
11	17	51	1.02	867	2.9	3.3
12	21	48	1.027	1008	4.0	4.0
	Av	erage		1145	2.9	2.7
	Std	. Dev.		312	0.6	0.9

Table 1
Analysis of adhesion data between PET substrate and Al coating.

data indicate that small buckling lengths result in high lateral compressive forces, with Point 12 exhibiting the highest force of 4.0×10^{-10} N at a buckling length of 48 µm. Moreover, Points 1, 3, 4, 5, and 6 have an average compressive force of 2.3×10^{-10} N at a buckling length of 60.2 µm. These findings confirm that buckling length directly affects lateral compressive force. Small buckling lengths correspond to high forces due to increased localized stress, whereas large buckling lengths lead to low compressive forces, indicating reduced stress and easy delamination.

The lateral compressive force (C) was calculated using the buckling frequency (n), the elastic modulus of Al (E), the moment of inertia of the Al coating (I), and the buckling delamination length (L). In this research, a tensile strain of 10% was applied. As shown in Fig. 3(c), the cross section of the Al coating was analyzed by SEM, and the coating thickness was measured with ImageJ, yielding an average thickness of $0.9 \, \mu m$.

Buckling delamination points, captured using a digital microscope [Fig. 3(d)], were analyzed to calculate the lateral compressive force. The buckling length and crack width for each numbered delamination point were measured. Using MATLAB for frequency analysis, and incorporating an elastic modulus of 70 GPa for Al and an average thickness of 0.9 μ m, we computed the lateral compressive force using Eq. (3). The results, presented in Table 1, indicate that the average lateral compressive force during buckling delamination was 2.9×10^{-10} N. The results revealed that small buckling lengths correspond to high lateral compressive forces. For Point 12, the highest lateral compressive force (4.0 \times 10⁻¹⁰ N) was observed at a buckling length of 48 μ m. For Points 2, 7, 8, 9, 10, and 11, the average lateral compressive force was 3.1×10^{-10} N at an average buckling length of 52.5 μ m. For Points 1, 3, 4, 5, and 6, the average lateral compressive force was 2.3×10^{-10} N at an average buckling length of 60.2 μ m.

These findings confirmed that small buckling lengths result in high compressive forces, indicating large stresses in those regions, which promotes coating deformation. Conversely, large buckling lengths were associated with low compressive forces, suggesting reduced stress and easy delamination.

Crack width also significantly impacted the lateral compressive force. For Point 1, buckling length = 50 μ m, crack width = 13 μ m, and compressive force = 2.4 \times 10⁻¹⁰ N. Despite a small buckling length, the small crack width resulted in a low compressive force. For Point 2, buckling length = 58 μ m, crack width = 25 μ m, and compressive force = 3.2 \times 10⁻¹⁰ N. A large crack width contributed to a high compressive force, even with a large buckling length.

To account for the combined effects of buckling length and crack width, the lateral compressive force per unit area was calculated to assess localized stress and delamination tendencies. The unit area was defined as the product of buckling length (L) and crack width (b). The lateral compressive force per unit area is expressed as

$$C = \frac{n^2 \pi^2 EI}{Lb}.$$
 (4)

As shown in Table 1, the average lateral compressive force per unit area was calculated as 2.7×10^{-13} N/ μ m². The analysis revealed that small unit areas correspond to high compressive forces per unit area. For group 1 (Points 1, 7, 8, 9, 11, and 12), the average compressive force per unit area was 3.5×10^{-13} N/ μ m², with an average unit area of 899 μ m². For group 2 (Points 2, 3, 4, 5, 6, and 10), the average compressive force per unit area was 1.9×10^{-13} N/ μ m², with an average unit area of 1390 μ m². These results demonstrated that regions with small unit areas experience large localized stresses, resulting in high compressive forces per unit area. In contrast, large unit areas distributed the stress evenly, leading to low compressive forces per unit area. This trend highlighted the impact of buckling and crack geometry on stress concentration and delamination behavior.

The analysis revealed that small unit areas correspond to high lateral compressive forces per unit area. This indicated that regions with small unit areas exhibit strong coating adhesion, as large forces were required to induce buckling delamination. Conversely, large unit areas resulted in low compressive forces per unit area, suggesting weak coating adhesion and easy delamination under buckling conditions. For Point 1, the lateral compressive force was 2.4×10^{-10} N, with a unit area of $650 \, \mu m^2$, resulting in a unit area compressive force of 3.7×10^{-13} N/ μm^2 . For Point 2, the lateral compressive force was 3.2×10^{-10} N, with a unit area of $1008 \, \mu m^2$, leading to a unit area compressive force of 2.2×10^{-13} N/ μm^2 . The key difference arose from the unit area size. Point 2, with its larger unit area, was more susceptible to delamination during buckling than Point 1. This highlighted the critical role of unit area in understanding coating behavior. By considering both buckling length and crack width to define unit area, the evaluation of coating adhesion became more comprehensive. This approach provided a clearer understanding of how adhesion strength and delamination resistance were affected by the geometric properties of the coating under lateral compressive forces.

3.4 Calculation results of lateral compressive force under tensile strain

In this experiment, we applied a tensile strain of 10%, after which the Al coating cross section was observed by SEM, as shown in Fig. 4(a). The thickness of the coating was measured with ImageJ, yielding an average of $0.7 \, \mu m$.

To calculate the lateral compressive force, the strain and strain rate data captured using a digital microscope were analyzed. As shown in Figs. 4(b)–4(d), buckling lengths and crack widths were measured at designated buckling points. These measurements were processed through frequency analysis in MATLAB. With the average coating thickness of 0.7 μ m and the Al elastic modulus of 70 GPa, all data were then substituted into the lateral compressive force equation [Eq. (3)] and the lateral compressive force per unit area equation [Eq. (4)] for the final calculations.

The results, summarized in Tables 2–4, correspond to tensile strains of 10, 15, and 20%, respectively. The calculated average lateral compressive forces are 3.1×10^{-10} , 3.2×10^{-10} , and 3.1×10^{-10} N, respectively. These findings demonstrate that the average lateral compressive force remains consistently around 3.0×10^{-10} N, regardless of the applied tensile strain during the buckling and delamination of the Al coating. At a tensile strain of 20%, the average lateral compressive force per unit area is 8.3×10^{-13} N/ μ m², higher than the values observed at tensile strains of 10 and 15%. This was due to the smaller average area of 421 μ m² at a tensile strain of 20%, which was lower than those at 10 and 15%. These findings suggested that the coating's adhesion per unit area was relatively enhanced under a tensile strain of 20%, compared with 10 and 15%.

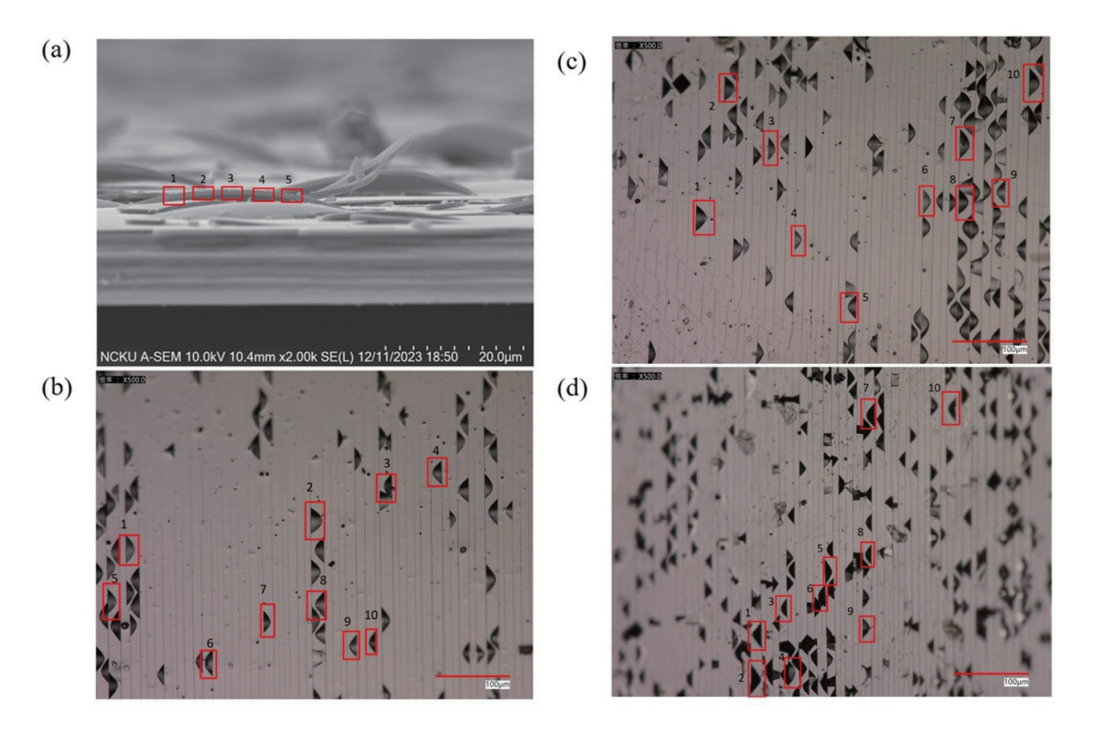


Fig. 4. (Color online) (a) SEM image showing secondary measurement locations for Al coating thickness. Calculation locations corresponding to tensile strains of (b) 10, (c) 15, and (d) 20%.

Table 2 Data analysis results of lateral compressive force at tensile strain of 10%.

ID	Width (µm)	Buckling length (µm)	Frequency	Area (μm²)	Compressive force (× 10 ⁻¹ N)	Unit area compressive force (× 10^{-1} N/ μ m ²)
1	16	37	0.990	592	2.3	3.8
2	18	35	1.067	630	3.3	5.2
3	16	35	1.022	560	2.7	4.8
4	15	31	1.009	465	3.1	6.7
5	16	32	1.018	512	3.2	6.2
6	14	35	0.997	490	2.2	4.6
7	13	27	1.028	351	3.7	10.6
8	18	34	1.031	612	3.3	5.3
9	14	31	1.066	434	3.3	7.5
10	13	27	1.037	351	3.8	10.8
		Average		500	3.1	6.6
Std. dev.				101	0.5	2.4

Table 3 Data analysis results of lateral compressive force at tensile strain of 15%.

ID	Width (µm)	Buckling length (μm)	Frequency	Area (μm²)	Compressive force (× 10 ⁻¹ N)	Unit area compressive force (× 10 ⁻¹ N/µm ²)
1	18	35	1.018	630	3.0	4.8
2	19	34	1.043	646	3.5	5.5
3	13	29	1.052	377	3.4	9.0
4	12	26	1.044	312	3.8	12.4
5	15	32	1.018	480	3.0	6.2
6	15	30	0.990	450	3.2	7.2
7	18	40	1.026	720	2.3	3.2
8	18	34	1.087	612	3.6	5.9
9	15	31	1.050	465	3.4	7.3
10	17	38	1.031	646	2.4	3.8
Average			534	3.2	6.5	
Std. dev.				135	0.5	2.7

Table 4 Data analysis results of lateral compressive force at tensile strain of 20%.

ID	Width (µm)	Buckling length (µm)	Frequency	Area (μm²)	Compressive force (× 10 ⁻¹ N)	Unit area compressive force (× 10 ⁻¹ N/μm ²)
1	16	34	1.036	544	2.9	5.4
2	17	42	1.022	714	2.0	2.8
3	11	24	1.039	264	4.1	15.4
4	13	30	0.987	390	3.1	7.9
5	11	33	1.005	363	2.0	5.5
6	15	29	1.031	430	3.7	8.6
7	15	32	1.055	480	3.2	6.7
8	11	25	1.001	275	3.5	12.7
9	12	26	0.988	312	3.4	11.0
10	14	31	1.028	434	3.0	7.0
		Average		421	3.1	8.3
		Std. dev.		136	0.7	3.8

4. Conclusions

In this research, we investigated the adhesion and mechanical stability of PVD Al coatings on PET substrates under tensile strain, with direct relevance to flexible and wearable sensor applications. By combining experimental observation with a buckling-delamination model based on Euler's critical load theory, we quantified lateral compressive forces and examined the effect of buckling geometry on adhesion performance. Results showed that tensile deformation induced shear-lag-driven crack formation and Poisson-effect-induced lateral compression, leading to buckling and delamination. Small buckling lengths and unit areas produced high compressive forces per unit area, indicating strong interfacial adhesion and high resistance to delamination, whereas large buckling geometries corresponded to reduced adhesion. Across all the strain levels tested, the average lateral compressive force remained at approximately 3.0×10^{-10} N, with the highest adhesion per unit area observed at a tensile strain of 20% due to reduced buckling area. These findings establish a practical framework for assessing adhesion in flexible metallic coatings, providing insights into the design of durable, strain-resistant sensor interfaces in next-generation flexible electronics.

Acknowledgments

This work was supported by the National Science and Technology Council, Taiwan (grant numbers 112-2221-E-006-173, 113-2221-E-006-087-MY2, 113-2221-E-006-112-MY2, 113-2221-E-006-116, and 114-2221-E-006-090). We gratefully acknowledge the Core Facility Center of National Cheng Kung University for providing access to the EM000700 equipment. We are also grateful for the partial support from the Higher Education Sprout Project, Ministry of Education, through the Headquarters of University Advancement at National Cheng Kung University (NCKU).

References

- 1 A. Gusain, A. Thankappan, and S. Thomas: J. Mater. Sci. **55** (2020) 13490. https://doi.org/10.1007/s10853-020-04883-1
- 2 S.-C. Shi, S.-T. Cheng, and D. Rahmadiawan: Sens. Actuators, A 379 (2024) 115981. https://doi.org/10.1016/j.sna.2024.115981
- 3 E. Luoma, M. Välimäki, and K. Immonen: J. Appl. Polym. Sci. **140** (2023) e53414.: https://doi.org/10.1002/app.53414
- 4 S. Skipidarov and M. Nikitin: Thin Film and Flexible Thermoelectric Generators, Devices and Sensors (Springer, 2021). https://doi.org/10.1007/978-3-030-45862-1
- 5 M. Gunda, P. Kumar, and M. Katiyar: Crit. Rev. Solid State Mater. Sci. 42 (2017) 129. https://doi.org/10.1080/10408436.2016.1186006
- 6 J. W. Hutchinson and Z. Suo: Advances in Applied Mechanics 29 (1991) 63. https://doi.org/S0065-2156(08)70164-9
- 7 M. J. Cordill, D. F. Bahr, N. R. Moody, and W. W. Gerberich: IEEE Trans. Device Mater. Reliab. 4 (2004) 163. https://doi.org/10.1109/TDMR.2004.829071
- 8 M. Humood, A. Asif, T. Guin, K. Polychronopoulou, J. C. Grunlan, and A. A. Polycarpou: Thin Solid Films 736 (2021) 138905. https://doi.org/10.1016/j.tsf.2021.138905
- 9 G. Mallikarjunachari and P. Ghosh: Polymer 90 (2016) 53. https://doi.org/10.1016/j.polymer.2016.02.042

- 10 G. Mallikarjunachari and G. Pijush: J. Appl. Polym. Sci. 133 (2016). https://doi.org/10.1002/app.43532
- M. J. Cordill, F. D. Fischer, F. G. Rammerstorfer, and G. Dehm: Acta Mater. 58 (2010) 5520. https://doi.org/10.1016/j.actamat.2010.06.032
- 12 M. J. Cordill, O. Glushko, and B. Putz: Front. Mater. 3 (2016) 11. https://doi.org/10.3389/fmats.2016.00011
- 13 S. Yu, X. Liu, Y. Sun, H. Zhou, and P. Cai: Thin Solid Films **669** (2019) 355. https://doi.org/10.1016/j.tsf.2018.11.021
- 14 K. Wu, J. Zhang, J. Li, Y. Wang, G. Liu, and J. Sun: Acta Mater. **100** (2015) 344. https://doi.org/10.1016/j.actamat.2015.08.055
- D. Rahmadiawan, S.-C. Shi, and W.-T. Zhuang: Mater. Res. Express 11 (2024) 115302. https://doi.org/10.1088/2053-1591/ad8f94
- 16 A. Amri, D. E. Putri, D. Febryza, S. D. Voadi, S. P. Utami, H. A. Miran, and M. M. Rahman: Teknomekanik 7 (2024) 139. https://doi.org/10.24036/teknomekanik.v7i2.32972
- 17 H. Nurdin, W. Waskito, A. N. Fauza, B. M. Siregar, and B. K. Kenzhaliyev: Teknomekanik 6 (2023) 94. https://doi.org/10.24036/teknomekanik.v6i2.25972
- 18 S.-C. Shi, T.-H. Chen, and P. K. Mandal: Polymers 12 (2020) 1246. https://doi.org/10.3390/polym12061246
- 19 C.-T. Chou, S.-C. Shi, and C.-K. Chen: Polymers 13 (2021) 4447. https://doi.org/10.3390/polym13244447
- 20 A. N. Fauza, F. Qalbina, H. Nurdin, A. Ambiyar, and R. Refdinal: Teknomekanik 6 (2023) 21. https://doi.org/10.24036/teknomekanik.v6i1.21472
- 21 N. Sandra, M. A. Caronge, J. Sunaryati, K. Kawaai, W. Nsama, Y. Arbi, and A. S. R. Arifin: Teknomekanik 8 (2025) 79. https://doi.org/10.24036/teknomekanik.v8i1.34572
- 22 S.-C. Shi, F.-I. Lu, C.-Y. Wang, Y.-T. Chen, K.-W. Tee, R.-C. Lin, H.-L. Tsai, and D. Rahmadiawan: Int. J. Biol. Macromol. 264 (2024) 130547. https://doi.org/10.1016/j.ijbiomac.2024.130547
- 23 H. Nurdin, W. Waskito, D. Harmanto, P. Purwantono, A. Kurniawan, D. Yuvenda, and Y. M. Anaperta: Teknomekanik 8 (2025) 24. https://doi.org/10.24036/teknomekanik.v8i1.33672
- 24 S. Yu, I. Goda, G. Parry, J. Durinck, Y. Ni, and C. Coupeau: Acta Mater. 283 (2025) 120505. https://doi.org/10.1016/j.actamat.2024.120505
- 25 X. Guan, A. P. Sarma, E. Kakarla Hamesh, J. Yang, N. Nguyen, E. Cerda, L. Pocivavsek, and S. S. Velankar: Int. J. Solids Struct. 254–255 (2022) 111843. https://doi.org/10.1016/j.ijsolstr.2022.111843